HHS Public Access

Author manuscript

Proc SPIE Int Soc Opt Eng. Author manuscript; available in PMC 2022 May 25.

Published in final edited form as:

Proc SPIE Int Soc Opt Eng. 2022 ; 11945: . doi:10.1117/12.2608975.

Creation of Non-Contact Device for Use in Metastatic Melanoma Margin Identification in *ex vivo* Mouse Brain

Matthew Tucker[a], **Matthew Lacayo**[c], **Suzanna Joseph**[b], **Weston Ross**[a,c], **Pakawat Chongsathidkiet**[c], **Peter Fecci**[c], **Patrick J Codd**[a,c]

[a]Duke University, Department of Mechanical Engineering and Materials Science, Durham, NC, USA

[b]Duke University School of Medicine, Durham, NC, USA

[c]Duke University School of Medicine, Department of Neurosurgery, Durham, NC, USA

Abstract

Because contemporary intraoperative tumor detection modalities, such as intraoperative MRI, are not ubiquitously available and can disrupt surgical workflow, there is an imperative for an accessible diagnostic device that can meet the surgeon's needs in identifying tissue types. The objective of this paper is to determine the efficacy of a novel non-contact tumor detection device for metastatic melanoma boundary identification in a tissue-mimicking phantom, evaluate the identification of metastatic melanoma boundaries in *ex vivo* mouse brain tissue, and find the error associated with identifying this boundary. To validate the spatial and fluorescence resolution of the device, tissue-mimicking phantoms were created with modifiable optical properties. Phantom tissue provided ground truth measurements for fluorophore concentration differences with respect to spatial dimensions. Modeling metastatic disease, ex vivo melanoma brain metastases were evaluated to detect differences in fluorescence between healthy and neoplastic tissue. This analysis includes determining required-to-observe fluorescence differences in tissue. H&E staining confirmed tumor presence in mouse tissue samples. The device detected a difference in normalized average fluorescence intensity in all three phantoms. There were differences in fluorescence with the presence and absence of melanin. The estimated tumor boundary of all tissue phantoms was within 0.30 mm of the ground truth tumor boundary for all boundaries. Likewise, when applied to the melanoma-bearing brains from *ex vivo* mice, a difference in normalized fluorescence intensity was successfully detected. The potential prediction window for the tumor boundary location is less than 1.5 mm for all *ex vivo* mouse brain tumors boundaries. We present a non-contact, laser-induced fluorescence device that can identify tumor boundaries based on changes in laser-induced fluorescence emission intensity. The device can identify phantom ground truth tumor boundaries within 0.30 mm using instantaneous rate of change of normalized fluorescence emission intensity and can detect endogenous fluorescence differences in melanoma brain metastases in *ex vivo* mouse tissue.

Keywords

Brain metastasis; Endogenous fluorescence; Warburg Effect; Tumor boundary detection; Melanoma

1. INTRODUCTION

Cancer is one of the leading causes of death worldwide with approximately 38.4% of individuals diagnosed with some form of cancer within their lifetime.[1] In 2020, there will be an estimated ~1.8 million new cancer diagnoses in the United States.[2] Approximately 30% of those 1.8 million will develop brain metastases at some point over their clinical course.[3] Over the last several decades, the identification and treatment of brain metastases has been refined and advanced. These advances include the incorporation of molecular profiling into the patient's prognosis after brain metastasis diagnosis, the adoption of stereotactic radiosurgery (SRS) as a treatment modality in conjunction with targeted therapies and the use of photonic solutions, such as laser interstitial therapy (LITT), to maximize tumor resection while minimizing morbidity.[4] However, despite these advancements in cancer diagnosis and treatment, there remains a poor prognosis for patients with brain metastases: a median survival time of 5–12 months and a 2.4% survival rate after 5 years.[5]

Contemporary treatment of brain metastasis often involves a multidisciplinarity across clinical disciplines, bearing a combination of surgical and non-surgical interventions. Surgical resection, combined with adjuvant treatment paradigms, including chemotherapy, immunotherapy and radiation therapy, form the cornerstone of current optimized treatment.[5] When surgical treatment is indicated, there is often a substantial survival benefit to maximizing the extent of safe tissue resection while preserving surrounding normal tissues.[6,7] The mechanical act of surgical resection requires the surgeon to precisely access the tumor within the normal anatomical structure during surgery. The current standard in localizing brain metastases involves the utilization of various imaging modalities — computed tomography, magnetic resonance imaging, angiography — in combination with an external reference system for computer-guided localization. In addition to these preoperative modalities, intraoperative methods such as intraoperative magnetic resonance imaging (iMRI), ultrasound and fluorescent probes and labels can be used to mark and identify pathologic tissue during surgery.[8,9]

Fluorescence-guided surgery (FGS) is a technique whereby fluorescent signals visualized during surgery aid the intraoperative identification and removal of tumorous tissue. FGS relies on utilizing a precisely characterized fluorophore and its emission spectrum of absorbed light. This allows discrimination between normal and pathologic tissue. FGS boasts an advantage to other tumor detection methods because it is relatively inexpensive. Additionally, the technique can be used intraoperatively without interrupting the surgical workflow.[10,11] FGS can be broadly divided into targeting one of two categories: exogenous and endogenous fluorophores. Exogenous fluorophores are molecules or agents that are introduced to the body that can subsequently be interrogated with the appropriate excitation light. Endogenous fluorophores are molecules already present in the body that have intrinsic fluorescence capabilities. This endogenous fluorescence is also known as autofluorescence.

Several exogenous fluorophores have been previously used intraoperatively to aid identification and removal of metastatic tumors in the brain. Specifically, brain tumor metastases originating from the lung, breast, colorectal tissue, and melanoma have been treated using FGS.[13] Fluorescein sodium is a common exogenous fluorophore that is

inexpensive and used in brain tumor surgery.[14–16] Once fluorescein sodium has been introduced to the patient, and has migrated to the tumor, the tumor can be visualized by exciting the area at 488 nm and collecting resultant emission at 500–550nm.[14] A study using fluorescein sodium in metastatic tumor resection by Okuda et al. (2010) determined that the use of fluorescein sodium has the potential to reduce local recurrence through improved extent of resection.[17]

Another common exogenous molecule used to aid in the identification of neurosurgical tumors is 5-Aminolevulinic acid (5-ALA). This drug was recently approved for use in the United States in 2017 for use in surgical tumor resection.[18] When 5-ALA is administered, it increases the concentration of a molecule called protoporphyrin IX (PpIX) in tumors.[19–21] The reason for this accumulation is hypothesized to be related to tumor-associated alterations, including affected heme biosynthetic enzymes, mitochondrial function and porphyrin transporters.[22] PpIX fluorescence is visible with peaks at 635 nm and 704 nm after excitation with 375–440 nm.[23,24] Use of 5-ALA during FGS has shown an increase of instances in complete resection of malignant gliomas compared to traditional white light microsurgery.[25] Despite the apparent utility of 5-ALA in the operating room, there exist concerns regarding transient neurologic deficits and temporary skin sensitivity.[26]

Endogenous fluorescence can also be used in FGS to detect the differences between healthy and tumor tissue.[4] The ability to differentiate these tissue types is based the Warburg effect whereby tumor cells have an elevated rate of glycolysis and lactic acid fermentation in the presence of oxygen.[27,28] Reduced nicotinamide adenine dinucleotide (NADH) and flavin adenine dinucleotide (FAD) differ in concentration as a result of these metabolic differences in healthy and tumor tissue.[29] Additionally, tissue properties such as absorption and scattering coefficient can differ. Because many of these molecules are also fluorophores, it is possible to use laser-induced fluorescence to detect differences in the fluorescence emission of these tissues.[29,30]

Previous studies have utilized endogenous fluorescence to differentiate healthy and tumorous tissue in *ex vivo* tissue. Liu et al. (2011) utilized a contact dependent laser induced fluorescence to differentiate mice with human glioblastoma tumor cells.[31] The contact-dependent laser was a laser-induced fluorescence device that featured a bifurcated fiber to both excite and collect resultant fluorescence emission. The excitation laser was a fiber-guided 407 nm laser and a spectrometer to measure fluorescence intensity. Although this device has many strengths, one major weakness is the need to make direct contact with the target tissue within the sterile field. This creates logistical hurdles regarding simultaneous surgical access and maintenance of the sterile surgical field to prevent infection.

Poulon et al. (2018) used two-photon microscopy and endogenous fluorescence to differentiate healthy tissue from glioblastoma and brain metastases.[32] These studies were completed on fresh, *ex vivo* human tissue using a multimodal two-photon microscope. Although this modality is useful for discerning tissue in a label-free method and does not require direct tissue contact, the large footprint of the two-photon microscope has the potential to restrict workflow in the operating room. These studies suggest that although endogenous fluorescence is a reliable, label-free way of aiding identification of brain

tumors, there remains is a need for a technology that can observe endogenous fluorescence without requiring contact to the surface and without a prohibitive footprint in the operating room.

In this study, we present a novel noncontact laser-induced fluorescence-based device, coined *TumorID,* that can distinguish between tumorous and healthy tissue. We discuss the implications for this device on intraoperative diagnostic methods for delineating healthy and tumor tissue to aid in surgical resection.

2. MATERIALS AND METHODS

2.1 Device Description

The device consists of a 405 nm fiber guided laser diode. The device utilized in the experiment is a compact, noncontact laser-induced fluorescence device (Figure 1).

The device consists of a 405 nm fiber guided laser diode (Thorlabs, Newton, NJ) to generate an excitation laser spot. The 425 nm long-pass dichroic mirror is positioned between the 0.20 NA objective lens and the achromatic doublet lens. All optical elements, including lenses and filters were purchased from Thorlabs, Newton, NJ. The $\frac{1}{e^2}$ diameter spot size of the laser 17 mm from the final optical element of the objective was 0.75 mm. The dichroic mirror reflects the incident laser light and allows the emission fluorescence greater than 425 nm to pass through the mirror to the achromatic doublet. The fluorescence passes through a 405 nm notch filter and is focused by the achromatic doublet into a fiber that leads to a CCD spectrometer (Thorlabs, Newton, NJ). The CCD spectrometer fiber has a core diameter of 200 mm. Figure 1b is an image of the experimental design used to collect data. In addition to the optical elements, the image also includes the labeled single-axis translation stage (Thorlabs, Newton, NJ) used to move samples relative to the TumorID. According to factory specifications, the translation stage can travel 25.4 mm, with a resolution of 25.4 mm. Synchronization of laser irradiation and CCD spectrometer is achieved using the PyVISA python module and the python programming language.

2.2 Tissue Phantom Design and Assembly

Tissue phantoms were used to mimic some of the molecular constituents and the fluorescence observed in healthy tissue and melanoma brain metastases. We have previously described many of the components of the solid tissue phantom design used in the study.[33] 1.2% w/v agarose (VWR International, Randor, PA) was an ingredient used to solidify the phantoms. The phantoms were designed with an absorption coefficient of 14 cm^{-1} and a reduced scattering coefficient of 200 cm^{-1}.[31] The absorption coefficient and scattering coefficient were achieved by using ferrous stabilized human hemoglobin (Sigma Aldrich, St. Louis, MO) to reach a final concentration of 31 mM and using a 20% intralipid emulsion (Baxter Healthcare, Deerfield, IL) to yield a final concentration of 2.5%.[31,34] The concentration of FAD and NADH were previously set to mimic concentrations found in human tissues.[31] The melanin concentration used in the experiment, 0.4%, is representative of the melanin concentration found in various melanomas.[35] Two extra phantoms were constructed to control for the presence of melanin and determine if changes in fluorescence

intensity were observable in the presence of melanin. Table 1 outlines the molecular components of each phantom.

Figure 2 illustrates the tissue phantom design used in the experiment. Figure 2a shows the general design of the tissue phantom. The phantom consists of a circular fiducial region, a healthy region and a circular tumor region. The dimensions for the fiducial regions, tumor region and distance between the fiducial and the tumor are included in Figure 2b. The diameter of the tumor region is 7.5 mm and the diameter of each fiducial 3.5 mm. The distance between the edge of the tumor and the edge of the fiducial is 3mm. The image of the 3D printed mold for the tissue phantom is pictured in Figure 2c. The 3D printed mold was created according to the specifications in Figure 2b. Figure 2d is an image of the full assembled phantom. The process of creating the phantom with the mold is outlined below.

Each phantom was constructed by placing the 3D printed phantom mold face down on a benchtop and pouring the healthy phantom material into the mold. In order to enable the healthy portion to be poured into the phantom, the solution was heated until the cloudy slurry became transparent. The solution was left in the mold for at least 15 minutes to cool and solidify. After the phantom solidified, the mold was removed from the phantom by lifting directly on the mold. After removing the mold, the solidified phantom was flipped. The solidified phantom contained 5 hollow cylinders in the phantom (4 fiducial cylinders and 1 tumor cylinder). The fiducial was a mixture of 1.2% w/v agarose and 3 mM Perylene-3,4,9,10-tetra-carboxylic dianhydride (PTCDA). The organic dye PTCDA (Sigma Aldrich, St. Louis, MO) was chosen because it does not diffuse well into the surrounding water agarose water matrix. The fiducial was inserted into each empty cylinder with a pipette until the solution filled the empty cylinder. The solution was allowed to cool, and the central tumor region was filled with a pipette.

2.3 Tissue Phantom Experiment

The assembled phantom was placed under the TumorID, and the laser spot is located to the left of the leftmost fiducial. The phantom was particularly placed, such that moving the stage and phantom relative to the TumorID bisects the eventual laser path of the three circles on the phantom (fiducial and tumor region). The phantom was moved in increments of 0.1 mm using the stage. The blue circles (not drawn to scale) in Figure 2d represent the outline of the laser spot irradiating the tissue. The black arrow also indicates the direction in which the laser spot moves relative to the phantom. A bandpass filter from 670–700 nm is used to detect the red color resulting from the fiducial. The current controlled laser intensity was set to 175 mA, and the spectrometer integration time is 0.8 ms. The spectrometer collected data throughout laser irradiation of the sample. The phantom continued to be moved in increments of 0.1 mm until the signal from the fiducial was not detected. For the next 51 measurements, the phantom was moved 0.25 mm between discrete measurements. Data were collected in triplicate for each position, waiting five seconds between measurements. Data were collected in triplicate and time was observed between measurements in an attempt to limit the occurrence of an erroneous intensity measurement. After 51 measurements, the phantom was again moved in increments of 0.1 mm. Signal within the bandpass is observed

and noted when the fiducial signal is detected and then subsequently not detected. This process was repeated for the other two phantoms.

2.4 Ex Vivo Mouse Brain Tissue Experiment

Two C57BL6 mice were used to model melanoma brain metastasis (B16F10). Mice were implanted with the tumor and developed for 10 days before being sacrificed.[36] Research that included mice was conducted under appropriate institutional IRB and animal handling approvals (Duke University IACUC A224–18-09). After sacrifice, the brain of the mouse was removed from the skull and placed on a glass slide. The explanted brains were then sectioned without fixation in the sagittal plane such that the cut passed through the melanoma tumor tissue based on direct visual inspection of the melanin staining correlating with the tumor location. The exposed tumor tissue was placed on a glass slide and placed underneath the TumorID. The device is positioned to the left of the exposed tumor and data collected through serial, adjacent applications of tissue irradiation at a controlled current of 185 mA for 0.8 seconds. Discrete points were measured until the 405 nm laser spot was visibly located to the right of the perceived lesion.

A 2D camera was focused on the slide such that the 405 nm laser spot was captured on the tissue sample to enable position to be correlated with position. Hematoxylin and Eosin (H&E) staining was conducted after the experiment. The remaining tissue was suspended in formalin and eventually embedded in paraffin. The paraffin-embedded samples were sectioned and stained by the Duke Research Immunohistology Lab.

2.5 Data Analysis and Curve Fitting

The recorded fluorescence emission versus position data were normalized using min-max normalization methods. The min-max normalization is achieved using the equation below.

$$x_{scaled} = \frac{x - x_{min}}{x_{max} - x_{min}} \tag{1}$$

Therefore, all intensity values were normalized between values of zero and one. The normalized data for each phantom and mouse was divided into two equal data sets. Each data set represents the left and right boundary for the object. A curve was fit to the data for both the left and right sides. The general logistic regression models used are listed below and the k and x0 terms solved for using non-linear least squares. MATLAB was used for the nonlinear curve fitting.

$$f(x)_{Right} = \frac{1}{1 + e^{-k(x - x_0)}} \tag{2}$$

$$f(x)_{Left} = \frac{1}{1 + e^{k(x - x_0)}} \tag{3}$$

Each resulting function was differentiated. These general functions, illustrated below, represent the instantaneous rate of change of normalized intensity for either the left or right side of the boundary.

$$f(x)_{Right} = \frac{ke^{-k(x-x_0)}}{\left(e^{-k(x-x_0)}+1\right)^2} \tag{4}$$

$$f(x)_{Left} = \frac{-ke^{-k(x-x_0)}}{\left(e^{k(x-x_0)}+1\right)^2} \tag{5}$$

The maximum instantaneous rate of change of normalized intensity is determined for both the right and left sides for phantoms and melanoma brain metastases. Additionally, for each phantom and mouse, the domain where the instantaneous rate of change of normalized intensity is 0% to 50% of the maximum was determined.

3. MATERIALS AND METHODS

3.1 Tissue Phantom Results

The normalized intensity versus position for each of the three phantoms are displayed in Figure 3. The ground truth for the left and right boundaries are labeled with a vertical red line on each of the subplots. The difference between the ground truth estimates were 7.40, 7.47, 7.57 mm for the melanoma-mimicking phantom, melanin (+) phantom, and melanin (−) phantom, respectively. For each of the generalized logistic regression models fit to the phantom intensity data, the coefficients of determination were all greater than 0.95.

The maximum instantaneous rate of change of intensity was determined for each of the three phantoms. The difference between the position where the maximum instantaneous rate of change of intensity occurs and the estimated ground truth are listed in Table 2. The difference between the two values for the melanoma-mimicking phantom was 0.27 mm for the left boundary and 0.14 mm for the right boundary. The same difference for (+) melanin phantom for the left boundary in 0.21 mm and 0.19 mm on the right. The difference for the (−) melanin phantom for the left boundary is 0.28 mm and 0.15 mm for the right boundary. Figure 4 shows the normalized intensity and instantaneous rate of change of normalized intensity versus position for the melanoma-mimicking phantom. The red dotted vertical line indicates where ground truth tumor boundary is located, and the black dotted vertical line indicates where the maximum instantaneous rate of change of normalized fluorescence intensity occurs.

Figure 12 shows how the size of the domain changes with respect to the percentage of the maximum instantaneous rate of change of normalized intensity. Figure 12a shows that size of the domain for the left tumor boundary, for mouse 1 and mouse 2, is less than 1 mm for 0% of the maximum. Figure 12b illustrates the size of the domain for the right tumor boundary, for mouse 1 and mouse 2, is less than 1 mm for ~25% of the maximum.

4. DISCUSSION

We were able to evaluate the detection of intensity differences for tissue phantoms, concluding that the TumorID can detect differences in endogenous fluorescence in the presence of melanin. The ground truth boundary estimates were within 0.2 mm of 7.5 mm. The differences in the prediction of finite tumor boundaries ranged from 0.14 mm to 0.28 mm, indicating that the normalized fluorescence intensity is a valid approach to represent the fine tumor boundary. Additionally, we investigated the use of prediction windows for TumorID data, showing that all prediction windows were equal to or less than 1 mm when at 33% of the maximum.

4.1 Detection of Intensity Differences for Tissue Phantoms

The brain metastasis melanoma-mimicking tissue phantom was used to illustrate the TumorID's capability to identify a melanoma brain metastasis in a mouse model. Figure 3 illustrates that there are two clear intensities detected for all phantoms, establishing that the TumorID can make that discrimination. A natural question is then whether the fluorescence detected was due to the presence of pigmented melanin absorbing the excitation and emission light or the endogenous fluorophore concentrations. Because there exist only two combinations of fluorophores in the phantom, it can be concluded that the TumorID can detect differences in endogenous fluorescence in the presence of melanin and that the resultant signal was not due to the pigmented absorption of melanin. This has important implications for the broader utility of the TumorID for classifying tumor types beyond melanoma including glial brain tumors, meningiomas, lymphomas or even other metastatic tumor subtypes.

4.2 Ground Truth Measurement

The difference between the ground truth boundary estimates were all within 0.2 mm of 7.5 mm. The diameter of the internal tumor circle is 7.5 mm. Therefore, with these data, we can conclude that the estimates of the tumor boundary location for the left and right boundaries are within 0.2 mm of the actual ground truth for the tissue phantom boundaries. The identification of these ground truth boundary measurements will enable further conclusions to be made regarding tumor boundary prediction using the TumorID.

4.3 Prediction of Finite Tumor Boundaries

The differences between the maximum instantaneous rate of change of normalized intensity and the ground truth for the tissue phantoms are reported in Table 2. The differences ranged from 0.13 mm to 0.28 mm. This result indicates that using the maximum instantaneous rate of change for normalized fluorescence intensity is a potential way to represent a finite tumor boundary. Because the maximum error is only slightly greater than the 0.10 mm step size used to move the laser spot to different part of the phantoms, it is likely that the difference between the two values is a result of the step size used in the experiment.

Figure 9 and figure 11 show how the maximum instantaneous rate of change of normalized fluorescence intensity align with the measurement location on the *ex vivo* mouse tissue for mouse 1 and mouse 2, respectively. A visual inspection reveals that these black dotted

lines coarsely align with the perceived melanoma brain metastasis lesion being measured. H&E staining revealed the presence of malignant cancer cells flanked by the healthy tissue on the left and right sides of this boundary. Due to changes in tissue hydration and dimensions associated with the fixation and staining process, conclusions concerning size and correlations to the results were not calculated. Future work will address how to incorporate quantitative measurements of animal tissue to evaluate the performance of the TumorID.

4.4 Calculation of a Prediction Window

As mentioned in previous sections, using the maximum instantaneous rate of change of normalized intensity for the laser induced fluorescence data collected can potentially be used as a method to identify the tumor margin in brain tumor metastases. However, there is a concern regarding the accuracy of a discrete measurement and potential failure. Rather than calculate a discrete prediction, we believe that range of values can be used to estimate the location of the tumor boundary.

A prediction window is defined as a range of values where the tumor boundary is predicted to be located. Figures 7 and 12 illustrate how the size of the prediction window decreases as the percentage of the maximum instantaneous rate of change of normalized intensity increases. For the tissue phantom experiments, the ground truth tumor boundary was contained within the prediction window calculated when percentages increased (up to 50%). All phantom prediction windows were equal to or less than 1 mm when at 33% of the maximum. The same trend where the prediction window decreases as the percentage of the maximum increases is revealed in figure 12 for the mouse data. Figure 12 reveals that the most significant decrease in prediction window size occurs between 0% and 10%.

The tumor boundary prediction window is much larger for the right-side boundary of mouse 1 versus the other three mouse tumor boundaries. When comparing this result to figure 9, the cause is likely associated with the fact that the line of laser spots is not perpendicular to the tumor boundary. Because the boundary is at an angle, relative to the TumorID, the signal versus distance is prolonged. To identify the cause for and later mitigate the larger boundary prediction window for one side over the other, an additional experiment could position the line of laser spots orthogonal to the tumor boundary.

Currently, surgical margins are determined with the surgeon’s experience, visual observation and neuronavigation. In fact, assessing surgical margins is rare and increasingly difficult due to time constraints and unreliable evaluation.[37] The accepted standard of practice is to resect within a 1 mm margin and with the TumorID’s ability to determine a margin that falls within that bound, we are not only able to systematically quantify margins for tumor resection but open discussion about what margin sizes in brain surgery can be tolerated and later identify practices to reduce intraoperative margins using the TumorID.

4.5 Potential TumorID Applications

The TumorID has the potential to be used in the operating room to intraoperatively identify the tumor boundary using fluorescence data. Our lab has previously developed a device that can remove tissue in an open-loop fashion.[38] This device, known as the TumorCNC, uses

CO_2 laser ablation to precisely remove soft tissue. The TumorID has the potential to close the loop for the TumorCNC and enable closed-loop tumor ablation based on intraoperative sensory data. Additionally, this technique would circumvent problems currently associated with FGS and intraoperative MRI regarding noncontact and small workflow footprint procedures.

Another potential application is using the TumorID to identify potential margins intraoperatively by hand. Because the TumorID is a noncontact system, with a long working distance, this device can collect data while minimizing potential contamination. Concerns for the device to be used by hand revolve around limitations concerning the oscillations, tremors, and precision of hand motion in surgery.[39,40] Therefore, the use of the TumorID with a robotic stabilizing system will likely lead to the most useful product.

4.6 Future Research Steps

Future research will aim to investigate if the detection error for the tumor boundary prediction can be decreased further. Being able to move the sample phantom with a motorized stage at a smaller step size, such as 0.05 mm, will provide data that will answer questions regarding step size and tumor boundary prediction error. Additionally, we will investigate the use of the device on other tumor types, such as different metastatic tumors, primary brain neoplasms such as glioblastoma multiforme (GBM), meningiomas or other intracranial pathology in order to determine comparable performance.

5. CONCLUSION

Maximal safe extent of resection when surgically removing brain metastases is an important factor in decreasing local reoccurrence. Available intraoperative feedback modalities, such as iMRI, are not ubiquitous across institutions, can be costly and often too costly and can interfere with the surgical workflow. Other fluorescence guided surgery methods require patient exposure to exogenous fluorescent compounds with associated side effects. Here we have presented a noncontact, laser induced fluorescence device, the TumorID, that can be used to identify the tumor boundary based on changes in laser induce fluorescence emission intensity. By using instantaneous rate of change of normalized fluorescence emission intensity, the TumorID can identify the location of the phantom ground truth tumor boundary within 0.3 mm. Additionally, the device was able to detect endogenous fluorescence differences in melanoma brain metastases in *ex vivo* mouse tissue. Future steps will include studying other tumor types, such as glial tumors and other metastatic lesions, and incorporating the device into robotic, or automated tumor removal systems.

REFERENCES

[1]. Cancer Statistics. https://www.cancer.gov/about-cancer/understanding/statistics. Accessed March 1, 2020.

[2]. Seigel RL, Miller KD, Jemal A. Cancer Statistics, 2020. CA: A Cancer Journal for Clinicians 2020 January 8; 70(1):7–30 [PubMed: 31912902]

[3]. Edwards MS, Boggan JE, Fuller TA. The Laser in Neurological Surgery. J Neurosurgy 1983;59(4):555–566.

[4]. Nagaya T, Nakamura YA, Choyke PL, Kobayashi H. Fluorescence-Guided Surgery. Front Oncol 2017; 7:314. Published 2017 Dec 22. doi:10.3389/fonc.2017.00314 [PubMed: 29312886]

[5]. Bhatia S, Tykodi SS, Thompson JA. Treatment of metastatic melanoma: an overview. Oncology (Williston Park) 2009;23(6):488–496. [PubMed: 19544689]

[6]. Agboola O, Benoit B, Cross P, et al. Prognostic factors derived from recursive partition analysis (RPA) of Radiation Therapy Oncology Group (RTOG) brain metastases trials applied to surgically resected and irradiated brain metastatic cases. Int J Radiat Oncol Biol Phys 1998;42(1):155–159. [PubMed: 9747833]

[7]. Tendulkar RD, Liu SW, Barnett GH, et al. RPA classification has prognostic significance for surgically resected single brain metastasis. Int J Radiat Oncol Biol Phys 2006;66(3):810–817. [PubMed: 17011454]

[8]. Hefti M Fluorescence-guided surgery for brain tumors. CNS Oncol 2013;2(1):67–74. doi:10.2217/cns.12.35 [PubMed: 25054357]

[9]. Jolesz FA. Intraoperative imaging in neurosurgery: where will the future take us? Acta Neurochir Suppl 2011;109:21–25. doi:10.1007/978-3-211-99651-5_4 [PubMed: 20960316]

[10]. Alander JT, Kaartinen I, Laakso A, et al. A review of indocyanine green fluorescent imaging in surgery. Int J Biomed Imaging 2012;2012:940585. doi:10.1155/2012/940585 [PubMed: 22577366]

[11]. Xi L, Jiang H. Image-guided surgery using multimodality strategy and molecular probes. Wiley Interdiscip Rev Nanomed Nanobiotechnol 2016;8(1):46–60. [PubMed: 26053199]

[12]. Kubben PL, ter Meulen KJ, Schijns OE, ter Laak-Poort MP, van Overbeeke JJ, van Santbrink H. Intraoperative MRI-guided resection of glioblastoma multiforme: a systematic review. Lancet Oncol 2011;12(11):1062–1070. doi:10.1016/S1470-2045(11)70130-9 [PubMed: 21868286]

[13]. Höhne J, Hohenberger C, Proescholdt M, et al. Fluorescein sodium-guided resection of cerebral metastases-an update. Acta Neurochir (Wien) 2017;159(2):363–367. doi:10.1007/s00701-016-3054-3 [PubMed: 28012127]

[14]. Diaz RJ, Dios RR, Hattab EM, et al. Study of the biodistribution of fluorescein in glioma-infiltrated mouse brain and histopathological correlation of intraoperative findings in high-grade gliomas resected under fluorescein fluorescence guidance. J Neurosurg 2015;122(6):1360–1369. [PubMed: 25839919]

[15]. Francaviglia N, Iacopino DG, Costantino G, et al. Fluorescein for resection of high-grade gliomas: A safety study control in a single center and review of the literature. Surg Neurol Int 2017;8:145. Published 2017 Jul 11. [PubMed: 28781922]

[16]. Okuda T, Kataoka K, Taneda M. Metastatic brain tumor surgery using fluorescein sodium: technical note. Minim Invasive Neurosurgery 2007;50(6):382–384. doi:10.1055/s-2007-993200

[17]. Okuda T, Kataoka K, Yabuuchi T, Yugami H, Kato A. Fluorescence-guided surgery of metastatic brain tumors using fluorescein sodium. J Clin Neurosci 2010;17(1):118–121. doi:10.1016/j.jocn.2009.06.033 [PubMed: 19969462]

[18]. Hadjipanayis CG, Stummer W. 5-ALA and FDA approval for glioma surgery. J Neurooncol 2019;141(3):479–486. doi:10.1007/s11060-019-03098-y [PubMed: 30644008]

[19]. Stepp H, Stummer W. 5-ALA in the management of malignant glioma. Lasers Surg Med 2018;50(5):399–419. doi:10.1002/lsm.22933 [PubMed: 29737540]

[20]. Otake M, Nishiwaki M, Kobayashi Y, et al. Selective accumulation of ALA-induced PpIX and photodynamic effect in chemically induced hepatocellular carcinoma. Br J Cancer 2003;89(4):730–736. doi:10.1038/sj.bjc.6601135 [PubMed: 12915887]

[21]. van der Beek N, de Leeuw J, Demmendal C, Bjerring P, Neumann HA. PpIX fluorescence combined with autofluorescence is more accurate than PpIX fluorescence alone in fluorescence detection of non-melanoma skin cancer: an intra-patient direct comparison study. Lasers Surg Med 2012;44(4):271–276. doi:10.1002/lsm.21134 [PubMed: 22170313]

[22]. Yang X, Palasuberniam P, Kraus D, Chen B. Aminolevulinic Acid-Based Tumor Detection and Therapy: Molecular Mechanisms and Strategies for Enhancement. Int J Mol Sci 2015;16(10):25865–25880. Published 2015 Oct 28. doi:10.3390/ijms161025865 [PubMed: 26516850]

[23]. Pogue BW, Gibbs-Strauss S, Valdés PA, Samkoe K, Roberts DW, Paulsen KD. Review of Neurosurgical Fluorescence Imaging Methodologies. IEEE J Sel Top Quantum Electron 2010;16(3):493–505. doi:10.1109/JSTQE.2009.2034541 [PubMed: 20671936]

[24]. Stummer W, Stepp H, Möller G, Ehrhardt A, Leonhard M, Reulen HJ. Technical principles for protoporphyrin-IX-fluorescence guided microsurgical resection of malignant glioma tissue. Acta Neurochir (Wien) 1998;140(10):995–1000. doi:10.1007/s007010050206 [PubMed: 9856241]

[25]. Hadjipanayis CG, Widhalm G, Stummer W. What is the Surgical Benefit of Utilizing 5-Aminolevulinic Acid for Fluorescence-Guided Surgery of Malignant Gliomas?. Neurosurgery 2015;77(5):663–673. doi:10.1227/NEU.0000000000000929 [PubMed: 26308630]

[26]. Smith J 5-Aminolevulinic Acid Hydrochloride (5-ALA HCl) for Oral Solution Oral presentation at: Medical Imaging Drugs Advisory Committee Meeting; May 10, 2017; Minneapolis, MN.

[27]. Smith J The benefits and challenges of medical-legal partnerships Oral presentation at: American Public Health Association Annual Meeting; June, 2011; Minneapolis, MN.

[28]. Vander Heiden MG, Cantley LC, Thompson CB. Understanding the Warburg effect: the metabolic requirements of cell proliferation. Science 2009;324(5930):1029–1033. doi:10.1126/science.1160809 [PubMed: 19460998]

[29]. Kolenc OI, Quinn KP. Evaluating Cell Metabolism Through Autofluorescence Imaging of NAD(P)H and FAD. Antioxid Redox Signal 2019;30(6):875–889. doi:10.1089/ars.2017.7451 [PubMed: 29268621]

[30]. Blacker TS, Duchen MR. Investigating mitochondrial redox state using NADH and NADPH autofluorescence. Free Radic Biol Med 2016;100:53–65. doi:10.1016/j.freeradbiomed.2016.08.010 [PubMed: 27519271]

[31]. Liu Q, Grant G, Li J, et al. Compact point-detection fluorescence spectroscopy system for quantifying intrinsic fluorescence redox ratio in brain cancer diagnostics. J Biomed Opt 2011;16(3):037004. doi:10.1117/1.3558840 [PubMed: 21456877]

[32]. Poulon Fanny, et al. “Real-time Brain Tumor imaging with endogenous fluorophores: a diagnosis proof-of-concept study on fresh human samples.” Scientific reports 8.1 (2018): 1–11. [PubMed: 29311619]

[33]. Tucker Matthew B., Wallace Catherine, Mantena Sreekar, Cornwell Neil, Ross Weston, Odion Ren, Vo-Dinh Tuan, Codd Patrick, “Creation of an optically tunable, solid tissue phantom for use in cancer detection,” Proc. SPIE 10480, Clinical and Translational Neurophotonics 2018, 104800H (8 February 2018); 10.1117/12.2290499

[34]. Flock ST, Jacques SL, Wilson BC, Star WM, van Gemert MJ. Optical properties of Intralipid: a phantom medium for light propagation studies. Lasers Surg Med 1992;12(5):510–519. doi:10.1002/lsm.1900120510 [PubMed: 1406004]

[35]. Watts Karen P., et al. “Melanin content of hamster tissues, human tissues, and various melanomas.” Cancer research 41.2 (1981): 467–472. [PubMed: 7448793]

[36]. Chongsathidkiet P, Woroniecka K, Dechant C, et al. BSCI-07. BONE MARROW T-CELL SEQUESTRATION IN THE SETTING OF BRAIN METASTASES. Neurooncol Adv 2019;1(Suppl 1):i2. Published 2019 Aug 12. doi:10.1093/noajnl/vdz014.006

[37]. Pirro V, Alfaro CM, Jarmusch AK, Hattab EM, Cohen-Gadol AA, Cooks RG. Intraoperative assessment of tumor margins during glioma resection by desorption electrospray ionization-mass spectrometry. Proc Natl Acad Sci U S A 2017;114(26):6700–6705. doi:10.1073/pnas.1706459114 [PubMed: 28607048]

[38]. Ross WA, Hill WM, Hoang KB, Laarakker AS, Mann BP, & Codd PJ (2018). Automating neurosurgical tumor resection surgery: Volumetric laser ablation of cadaveric porcine brain with integrated surface mapping. Lasers in surgery and medicine, 50(10), 1017–1024. [PubMed: 29984837]

[39]. Fargen KM, Turner RD, & Spiotta AM (2016). Factors that affect physiologic tremor and dexterity during surgery: a primer for neurosurgeons. World neurosurgery, 86, 384–389. [PubMed: 26585718]

[40]. Camarillo DB, Krummel TM, & Salisbury JK Jr (2004). Robotic technology in surgery: past, present, and future. The American Journal of Surgery, 188(4), 2–15.

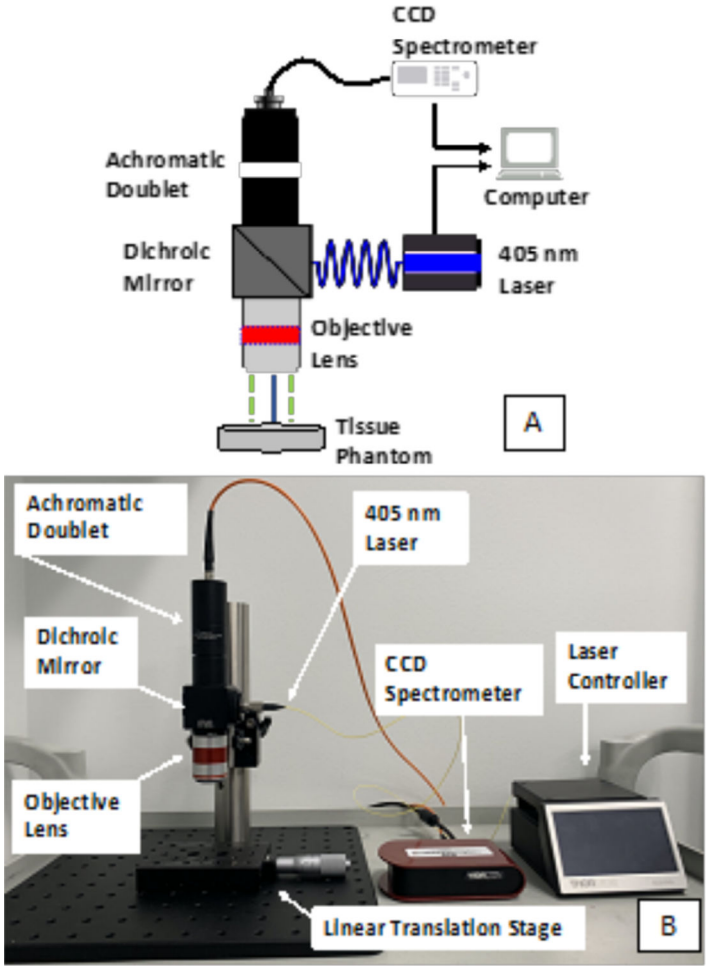

Figure 1.

A) Illustration of the optical components for the TumorID. B) Image of the experimental design for the TumorID linear stage.

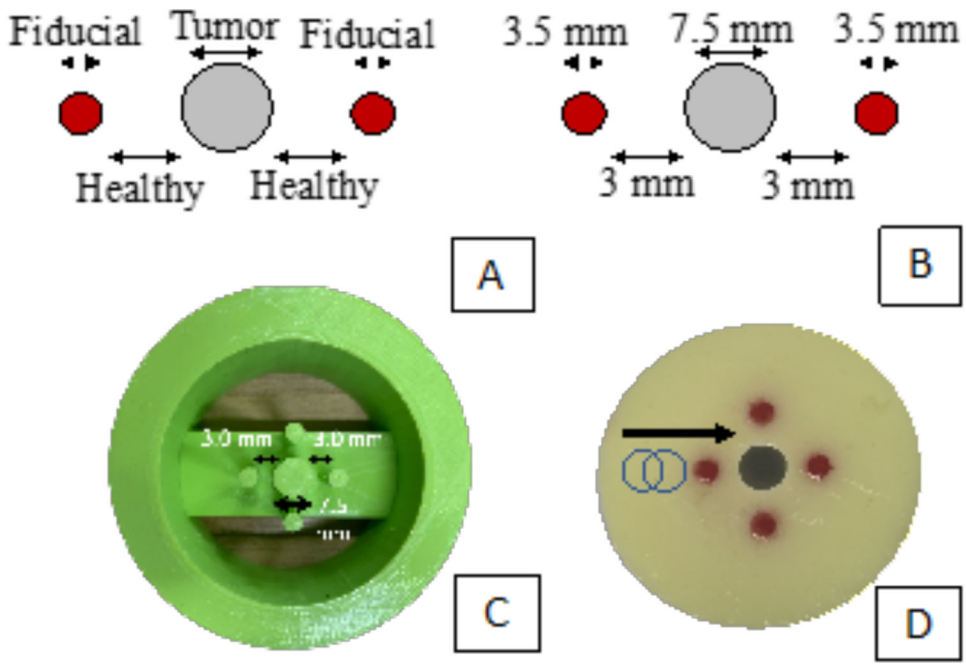

Figure 2.

A) General outline for the phantom model showing that the fiducials are separated by the tumor by healthy tissue phantom B) The distance and size measurements for the phantom model C) Image of 3D printed mold used to create phantoms D) Completed phantom with blue circle representing laser spots and a black arrow indicating the direction of information sampling (not to scale)

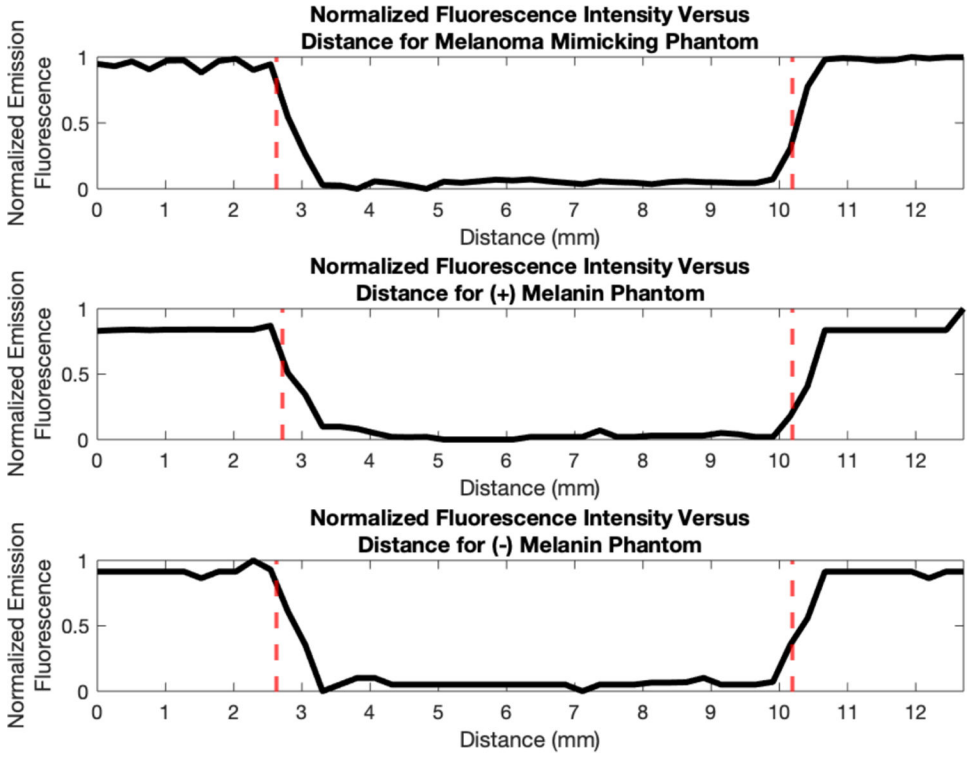

Figure 3).

Normalized fluorescence plotted versus the location on the solid tissue phantom for all three phantom models.

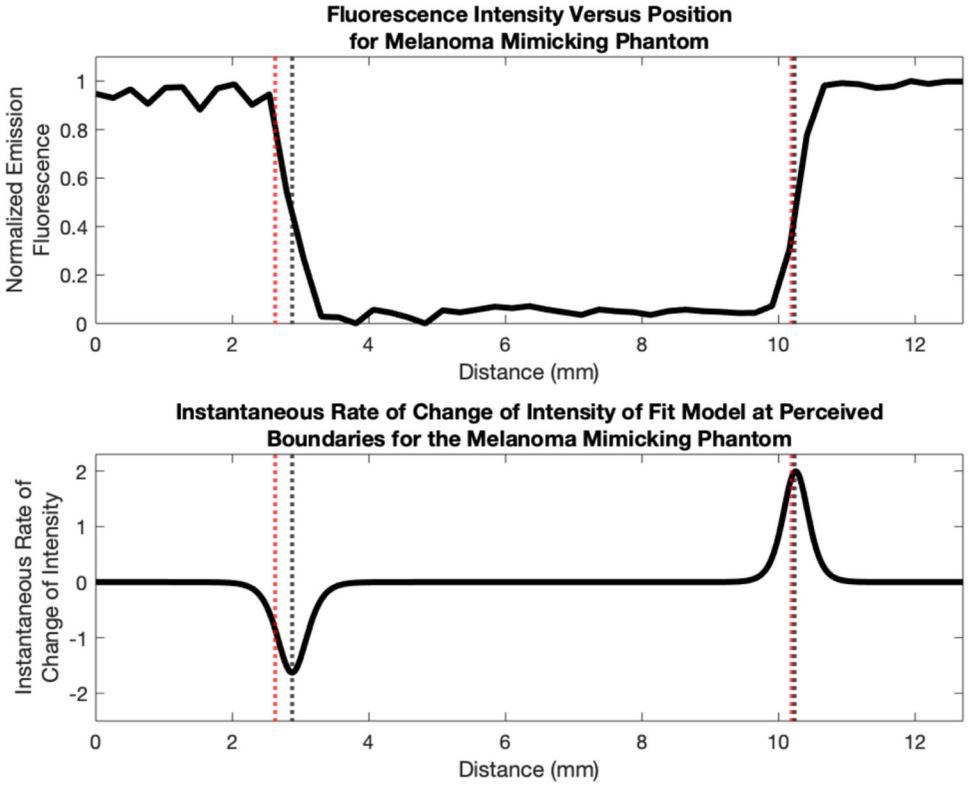

Figure 4).

The ground truth tumor boundary (in red) and maximum instantaneous rate of change (black) plotted on figures of normalized fluorescence emission and instantaneous rate of change of fluorescence emission.

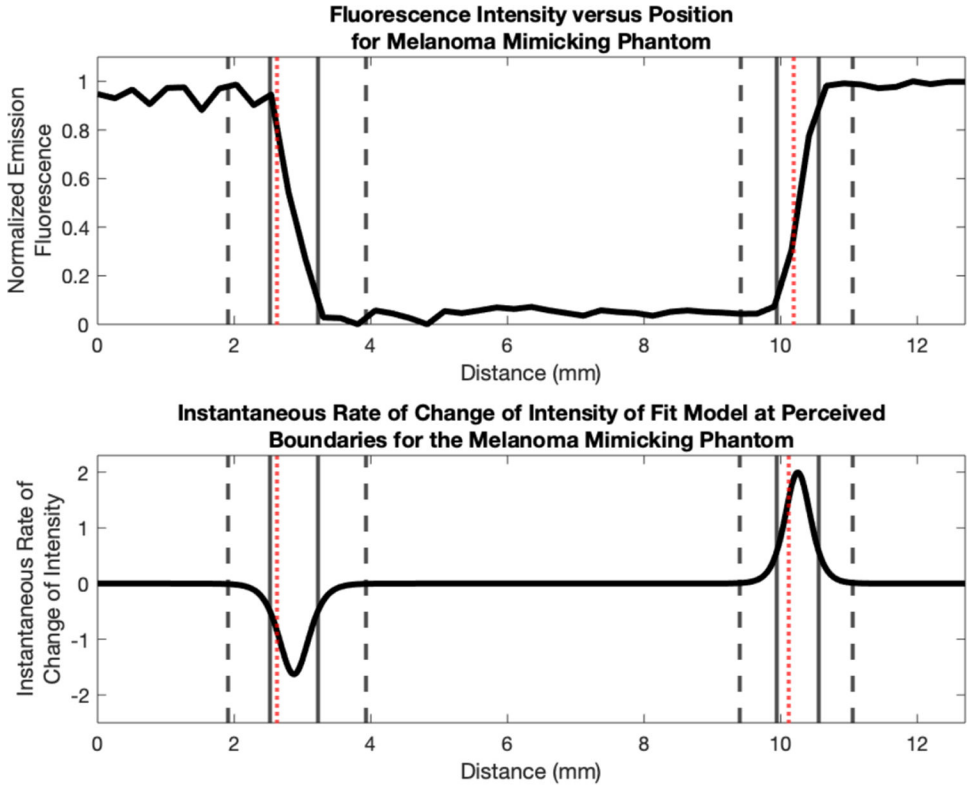

Figure 5).

Prediction windows for domain encompassing 0%(dashed) and 30%(solid) of the maximum intensity. The red dotted line represents the ground truth of the tumor boundary. This figure illustrates the size of the domain that encompasses 0% and 30% of the maximum intensity of the instantaneous rate of change for normalized fluorescence intensity. The dashed black line illustrates the size of the domain where at least 0% of the maximum is included. The solid line indicates where at least 30% of the maximum is included.

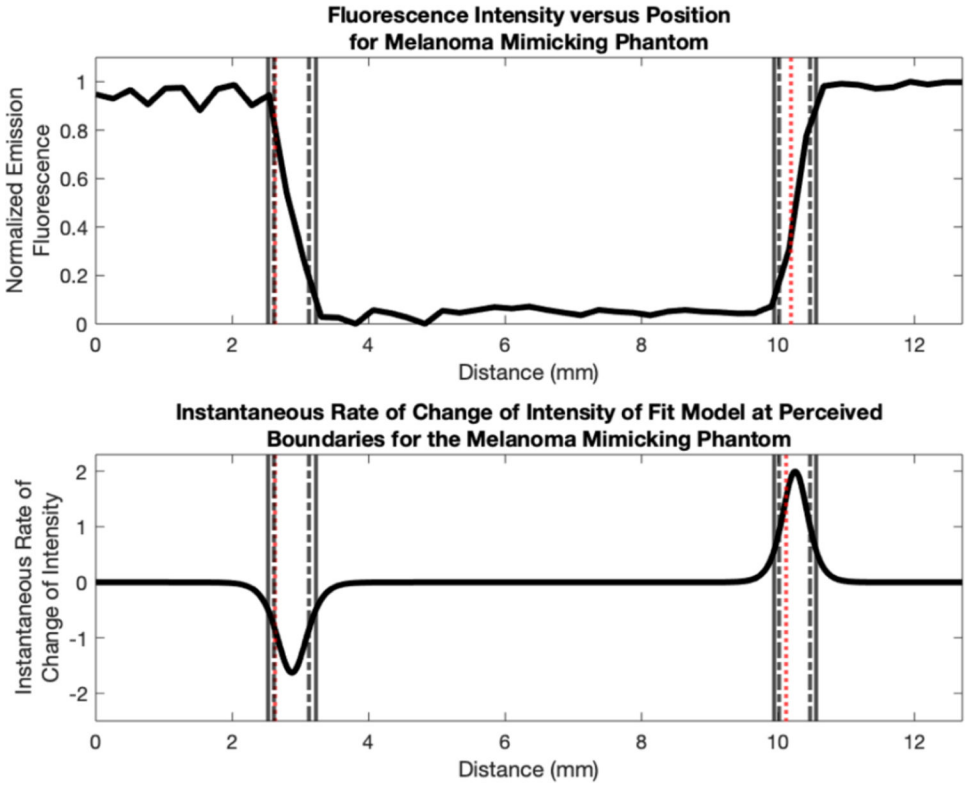

Figure 6).

Prediction windows for domain encompassing 30%(solid) and 50%(dashed-dotted) of the maximum intensity. The red dotted line indicates the tumor ground truth. The red dashed line represents the ground truth of the tumor boundary. This figure illustrates the same melanoma mimicking figures as Figure 5. However, in this figure, the solid line indicates where 30% of the maximum is included and the dashed-dotted line indicates where at least 50% of the maximum is included.

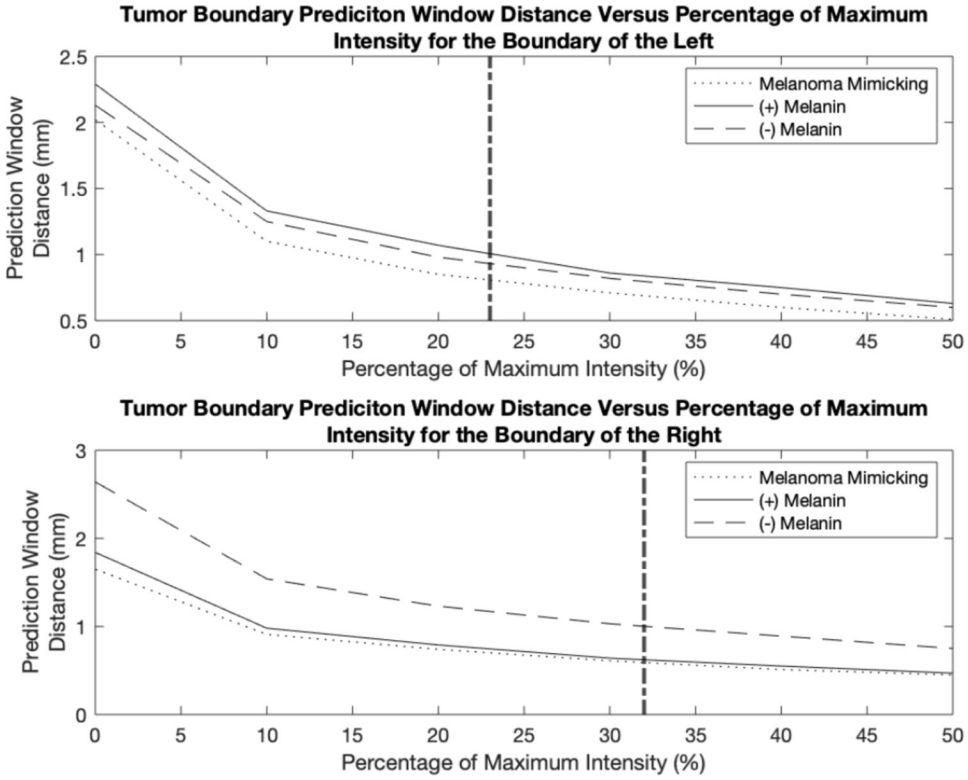

Figure 7).

The size of the prediction window, as a function of the percentage of maximum instantaneous rate of change of intensity, for the left and right boundaries (dotted-dashed line represents where prediction window is less than 1 mm). The relationship between the size of the domain versus the percentage of the maximum intensity is observed for all three phantoms. Figure 7a includes the left side of the phantom and the right side. The vertical line is positioned at 23% of the maximum for the left tumor boundary and 33% for the right side of the tumor boundary.

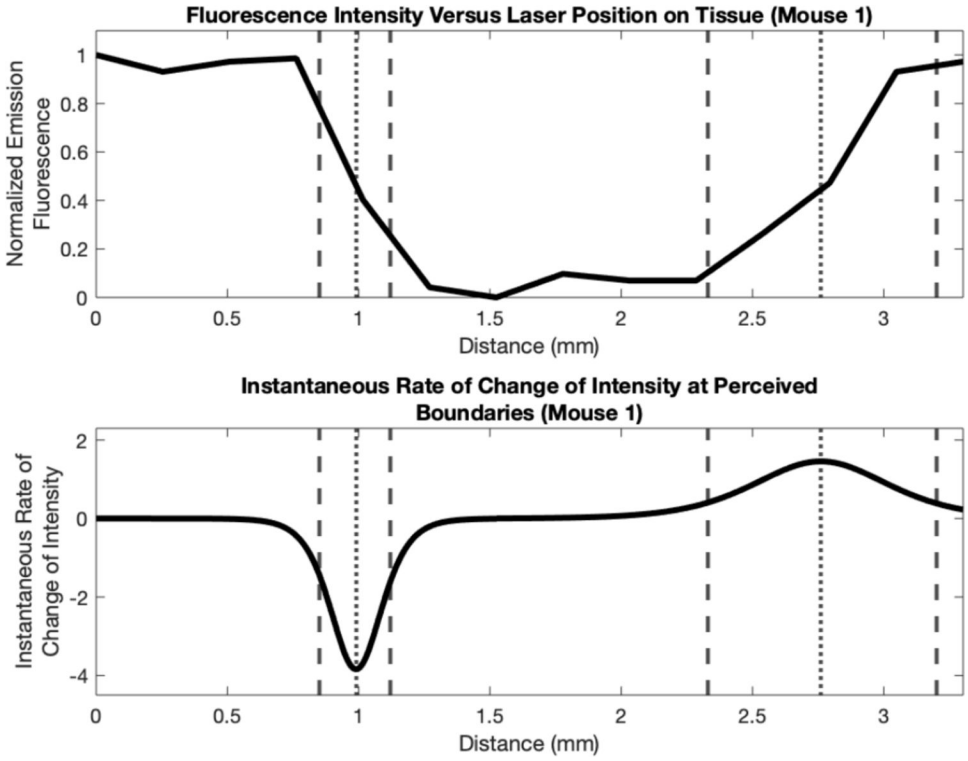

Figure 8).

Prediction windows of mouse 1 for domain encompassing 35%(dashed) of the maximum intensity. The black dashed line represents the maximum instantaneous rate of change of fluorescence emission. The bottom image shows the instantaneous rate of change of normalized fluorescence intensity. The black dotted line illustrates the maximum instantaneous rate of change of normalized fluorescence intensity. The black dashed line indicates the domain where at least 35% of the maximum value is contained.

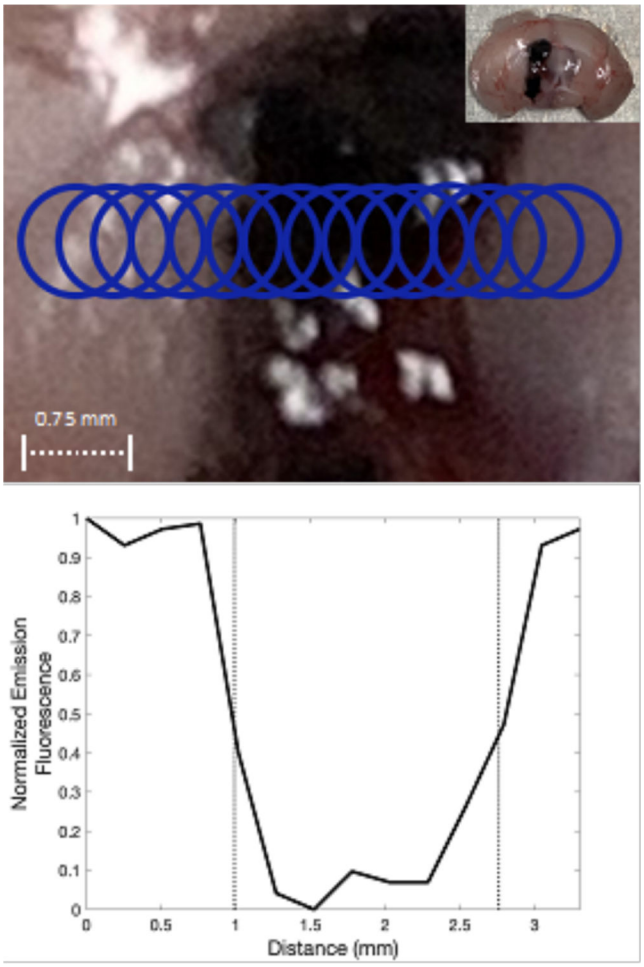

Figure 9).

(Top) Scaled image focused on the melanoma brain metastasis lesion of the mouse 1 tissue sample with blue circles outlining where the laser spot collected data. The small image inlaid in the top right corner shows the entire brain sample from the mouse. (Bottom) A graph of the normalized fluorescence intensity plotted versus position. The black dotted line denotes where the instantaneous rate of change of fluorescence intensity is greatest.

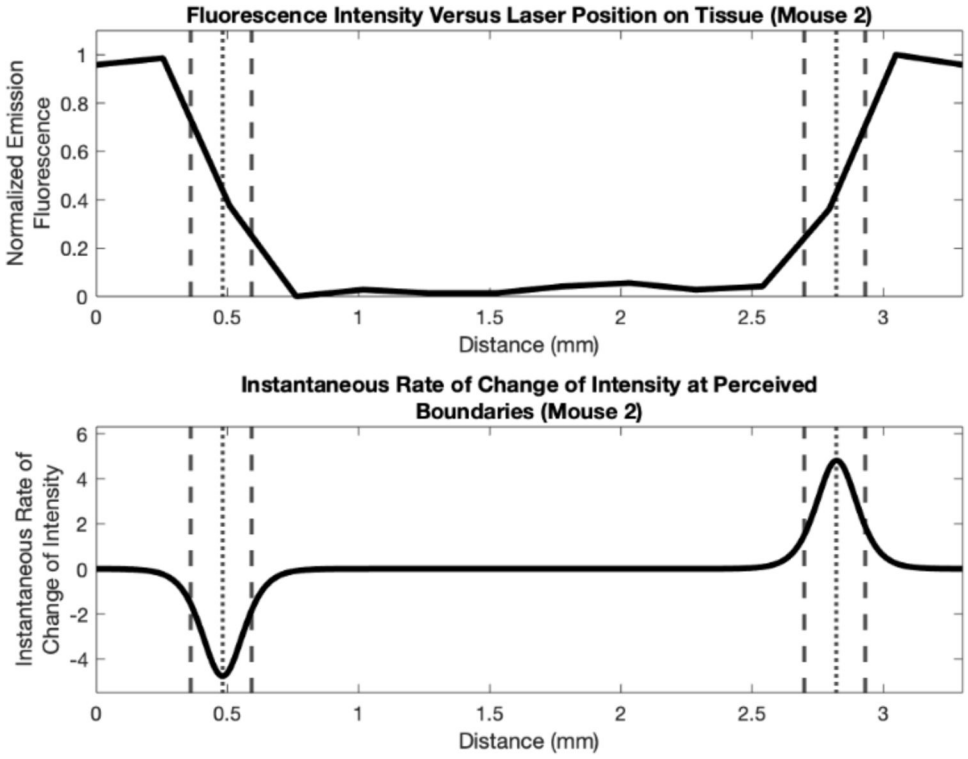

Figure 10).

(Top) Prediction windows of mouse 2 for domain encompassing 35%(dashed) of the maximum intensity. (Bottom) The instantaneous rate of change of normalized fluorescence intensity. The black dashed line represents the maximum instantaneous rate of change of fluorescence emission

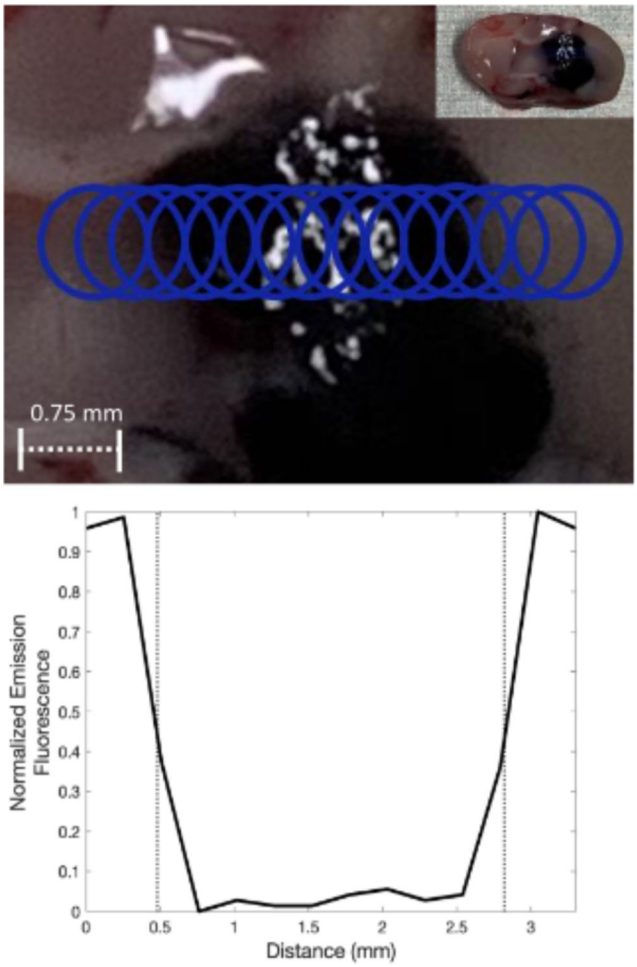

Figure 11).

(Top) Scaled image that uses blue circles to represent the laser irradiation spot versus the tissue position. The small image inlaid in the top right corner shows the entire brain sample from the mouse. (Bottom) A graph of normalized fluorescence intensity versus position for the blue circles aligned with the mouse 2 image. The black dotted line denotes where the instantaneous rate of change of fluorescence intensity is greatest.

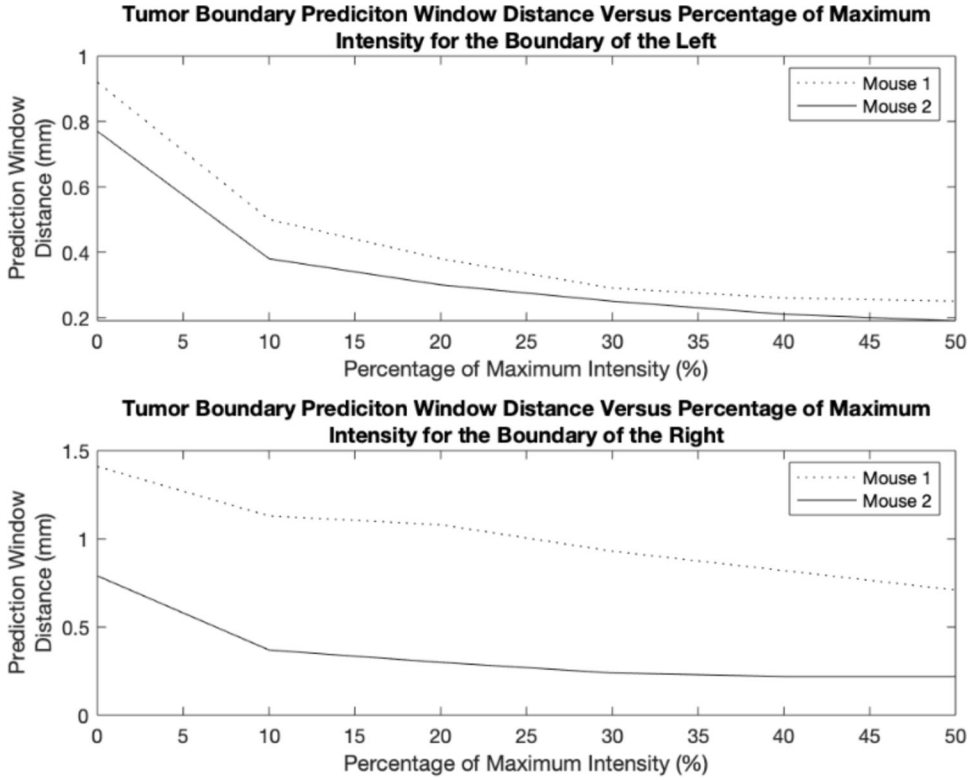

Figure 12).

The size of the prediction window for mouse 1 and 2, as a function of the percentage of maximum instantaneous rate of change of intensity, for the left and right boundaries

Table 1)

The molecular composition of the three phantom types: melanoma-mimicking, + melanin and − melanin. Each "X" indicates the presence of that phantom constituent.

	Phantom Constituent					
	2.5% Intralipid	**31μM Hemoglobin**	**1.6 μM FAD**	**16 μM FAD**	**1.25mM NADH**	**Melanin**
Melanoma Mimicking Phantom						
Inside	**X**	**X**	**X**		**X**	**X**
Outside	**X**	**X**		**X**	**X**	
(+) Melanin Phantom						
Inside	**X**	**X**	**X**		**X**	**X**
Outside	**X**	**X**		**X**	**X**	**X**
(−) Melanin Phantom						
Inside	**X**	**X**	**X**		**X**	
Outside	**X**	**X**		**X**	**X**	

Table 2)

The average distance on the left boundary, average distance on the right boundary and respective standard deviations for the three phantom types: melanoma-mimicking, + melanin and − melanin.

	Average Distance on the Left (mm)	Standard Deviation on the left (mm)	Average Distance on the Right (mm)	Standard Deviation on the Right (mm)
Melanoma Mimicking	0.27	0.09	0.14	0.10
(+) Melanin	0.21	0.13	0.19	0.12
(−) Melanin	0.28	0.04	0.15	0.05